APL Materials

AIP Publishing

RESEARCH ARTICLE | APRIL 14 2023

Understanding the phase transition mechanism in the lead halide perovskite $CsPbBr_3$ via theoretical and experimental GIWAXS and Raman spectroscopy

Alexander E. J. Hoffman ; Rafikul Ali Saha ; Sander Borgmans ; Pascal Puech ; Tom Braeckevelt ; Maarten B. J. Roeffaers ; Julian A. Steele ; Johan Hofkens ; Veronique Van Speybroeck

APL Mater 11, 041124 (2023)

https://doi.org/10.1063/5.0144344

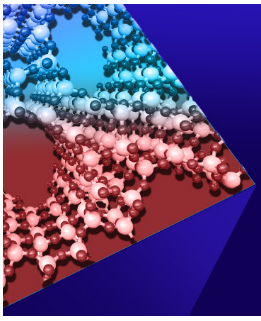

APL Materials ARTICLE scitation.org/journal/apm

Understanding the phase transition mechanism in the lead halide perovskite $CsPbBr_3$ via theoretical and experimental GIWAXS and Raman spectroscopy

Cite as: APL Mater. **11**, 041124 (2023); doi: 10.1063/5.0144344
Submitted: 29 January 2023 • **Accepted:** 4 April 2023 •
Published Online: 14 April 2023

Alexander E. J. Hoffman,[1] **Rafikul Ali Saha,**[2] **Sander Borgmans,**[1] **Pascal Puech,**[3] **Tom Braeckevelt,**[1,a)] **Maarten B. J. Roeffaers,**[2] **Julian A. Steele,**[2,b)] **Johan Hofkens,**[4,c)] **and Veronique Van Speybroeck**[1,d)]

AFFILIATIONS

[1] Center for Molecular Modeling, Ghent University, Technologiepark 46, 9052 Zwijnaarde, Belgium
[2] cMACS, Department of Microbial and Molecular Systems, KU Leuven, Celestijnenlaan 200F, 3001 Leuven, Belgium
[3] Centre d'Elaboration des Matériaux et d'Etudes Structurales (CEMES), UPR8011 CNRS, Université Toulouse 3, Rue Jeanne Marvig 29, 31055 Toulouse, France
[4] Department of Chemistry, KU Leuven, Celestijnenlaan 200F, 3001 Leuven, Belgium

[a)] Also at: Department of Chemistry, KU Leuven, Celestijnenlaan 200F, 3001 Leuven, Belgium.
[b)] Also at: School of Mathematics and Physics, The University of Queensland, Brisbane, QLD 4072, Australia. julian.steele@kuleuven.be
[c)] Also at: Max Plank Institute for Polymer Research, Ackermannweg 10, D-55128 Mainz, Germany. johan.hofkens@kuleuven.be
[d)] **Author to whom correspondence should be addressed:** veronique.vanspeybroeck@ugent.be

ABSTRACT

Metal-halide perovskites (MHPs) exhibit excellent properties for application in optoelectronic devices. The bottleneck for their incorporation is the lack of long-term stability such as degradation due to external conditions (heat, light, oxygen, moisture, and mechanical stress), but the occurrence of phase transitions also affects their performance. Structural phase transitions are often influenced by phonon modes. Hence, an insight into both the structure and lattice dynamics is vital to assess the potential of MHPs. In this study, GIWAXS and Raman spectroscopy are applied, supported by density functional theory calculations, to investigate the apparent manifestation of structural phase transitions in the MHP $CsPbBr_3$. Macroscopically, $CsPbBr_3$ undergoes phase transitions between a cubic (α), tetragonal (β), and orthorhombic (γ) phase with decreasing temperature. However, microscopically, it has been argued that only the γ phase exists, while the other phases exist as averages over length and time scales within distinct temperature ranges. Here, direct proof is provided for this conjecture by analyzing both theoretical diffraction patterns and the evolution of the tilting angle of the $PbBr_6$ octahedra from molecular dynamics simulations. Moreover, sound agreement between experimental and theoretical Raman spectra allowed to identify the Raman active phonon modes and to investigate their frequency as a function of temperature. As such, this work increases the understanding of the structure and lattice dynamics of $CsPbBr_3$ and similar MHPs.

I. INTRODUCTION

Perovskites can contribute to the transition toward a sustainable economy as they are promising materials for solar cells[1–4] and other energy conversion devices.[5] In recent years, their power conversion efficiency has been increased from 3.8% in 2009[6] to more than 25%,[7,8] making them competitive with established solar technologies. Perovskites have a typical chemical formula of ABX_3, where A and B are both cations with different atomic radii and the X site is taken by an anion. The A cations are centrally placed between the B cations, which, in turn, are located in the centers of BX_6 octahedra.

A specific subclass of perovskites, the metal-halide perovskites (MHPs), has been the center of research lately.[9,10] In MHPs, the A site is represented by an organic or inorganic monovalent cation such as methylammonium (MA), formamidinium (FA), Cs, or Rb. The B site is occupied by a divalent metal cation such as Pb or Sn. Finally, the X site is filled by a halide anion, typically Cl, Br, or I. With regard to optoelectronic applications, MHPs show suitable properties such as tunable direct bandgaps, high intrinsic carrier mobilities, long carrier lifetimes, high photoluminescence lifetimes and yields, and high defect tolerance.[9–13] Despite these advantages, the bottleneck of incorporating MHPs in present-day devices is the lack of long-term operational stability.[9,14] In addition to the degradation of the material due to heat, light, oxygen, moisture, and mechanical stress,[15–18] MHPs exhibit phase transitions under operating conditions, which can also have an impact on their optoelectronic properties.[17,19–21] These phase transitions are the result of structural fluctuations induced by soft phonon modes.[22] With an eye toward future commercialization, it is important to understand the relation between these phonon modes, the phase transition mechanism, and the influence on essential material properties.

Phonon modes have been extensively studied in MHPs already because of their link with structural phase transitions.[23–44] Usually, molecular simulations are required to gain an insight into the phonon modes that are involved. With the help of a simple theoretical picture, it is possible to identify important phonon modes in the phonon band structure obtained via normal mode analysis following static DFT calculations. As an illustration, we consider the phonon band structures of the three macroscopic phases of the MHP $CsPbBr_3$ (see Fig. 1). The choice for $CsPbBr_3$ is inspired by the lack of organic parts, which simplifies the spectral analysis and allowed us to focus on the low-frequency phonon spectrum only. Moreover, inorganic MHPs are more stable under atmospheric conditions, which make them experimentally more tractable.[45] Furthermore, $CsPbBr_3$, in contrast to the more popular $CsPbI_3$, does not exhibit a photo-inactive δ phase,[46–48] which again facilitates the experimental characterization. At high temperatures (above 403 K), $CsPbBr_3$ appears in its highly symmetric cubic α phase,[49] whereas at low temperatures (below 361 K), the structure is in its lower symmetry orthorhombic γ phase.[49] The tetragonal β phase is present at intermediate temperatures.[49]

As shown in Fig. 1, the phonon band structure of the γ phase of $CsPbBr_3$ contains merely positive phonon bands, indicating that this phase is located in a minimum of the potential energy surface and, consequently, is stable at 0 K. In contrast, in the phonon band structures of the α and β phases, there exist phonon modes with imaginary frequencies at several points in the first Brillouin zone (here presented by negative phonon frequencies), clearly showing that these phases are intrinsically unstable at 0 K.[50] This is a general feature of MHPs and is in agreement with literature reports.[35–39,41–44] Moreover, the phonon modes with imaginary frequencies indicate in which way the structure can be deformed to reach an energetically more favorable state. On the one hand, the instability at the M-point in the α phase is the result of in-phase tilting of the $PbBr_6$ octahedra. This kind of tilting leads to a transition to the β phase. On the other hand, the instability at the R-point in the cubic α phase and the Z-point in the tetragonal β phase is caused by out-of-phase tilting of the $PbBr_6$ octahedra. Starting from the β phase, this out-of-phase tilting around both the x- and y-axes, in combination with Cs displacements in the x and y directions, gives rise to a transition to the γ phase.[33]

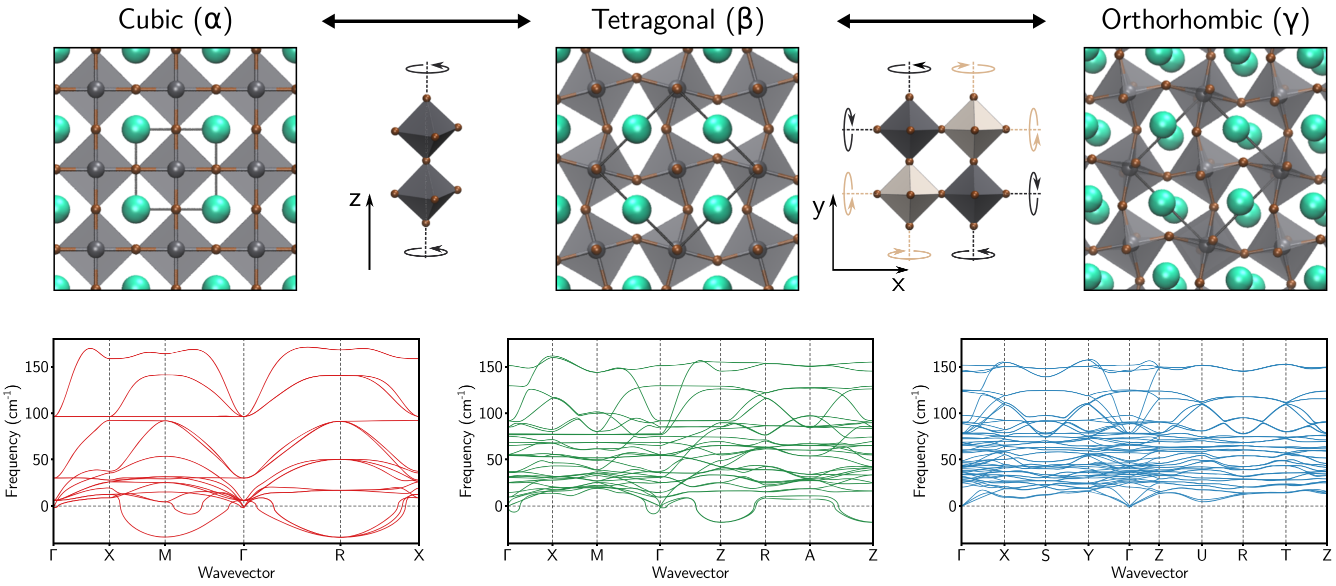

FIG. 1. Visualization of the cubic, tetragonal, and orthorhombic phases of $CsPbBr_3$. The in-phase tilting along the z-axis transforms the cubic phase into the tetragonal phase. The out-of-phase tilting along the x- and y-axes transforms the tetragonal phase into the orthorhombic phase. The phonon band structures of the different structures are shown at the bottom. The cubic phase has imaginary phonon modes around the M- and R-points at the border of its first Brillouin zone. The tetragonal phase has imaginary phonon modes around the Z-point of its first Brillouin zone.

The above-mentioned normal mode analysis, which is inherently harmonic, demonstrates why $CsPbBr_3$ resides in its γ phase at low temperatures. However, as phonon modes in MHPs are strongly anharmonic,[26,38,39] this harmonic theory breaks down at realistic temperatures. Hence, it cannot explain the phase transition mechanism. Anharmonic phonon modes can behave as soft modes, whose frequency decreases toward zero when the phase-transition temperature is approached. These modes drive displacive phase transitions, as is the case in several types of perovskites such as $SrTiO_3$[51] and $Cs_2AgBiBr_6$.[52] In the case of $CsPbBr_3$, the phase transitions have a different origin as such soft modes have not been observed. Recently, there are reports that the pure tetragonal and cubic phases do not actually exist on a local scale. Instead, static and dynamic disorder in the structure makes them appear as averages over longer time and length scales.[29,37,40,41,52–57] Dynamic disorder originates from transitions between different lower-symmetry systems, which yields, on average, a highly symmetric system. In the case of $CsPbBr_3$, these transitions are governed by phonon modes inducing octahedral tilting in the orthorhombic phase. The dynamics of this phenomenon can be described by an anharmonic multi-well potential energy surface.[41] When the temperature increases, the energy barrier of specific paths between different symmetry equivalent orthorhombic states can be crossed. This can explain the observed order of phase transitions: one of these paths, leading to a time-averaged tetragonal phase, has a significantly lower-energy barrier than the others. When crossing this energetic barrier at the phase-transition temperature, the tetragonal phase is observed. The other paths lead to a time-averaged cubic phase once their energetic barrier is overcome.[41]

In this work, the hypothesis of dynamic disorder leading to the tetragonal and cubic phases is further corroborated by grazing-incidence wide-angle x-ray scattering (GIWAXS) and Raman spectroscopic measurements supported by theoretical simulations on $CsPbBr_3$. GIWAXS is a popular technique to characterize the structure of MHP thin films,[58] whereas Raman spectroscopy has already showed its value in the characterization of the lattice dynamics of $CsPbBr_3$.[29,30,52,59–63] For instance, an important contribution by Yaffe *et al.* dedicated the origin of the Raman central peak (i.e., at 0 cm^{-1}) to polar fluctuations due to head-to-head motions of the Cs atoms, coupled with perpendicular, outward motion of the neighboring Br atoms.[29] Later on, Gao *et al.* showed that octahedral tilting contributes to the Raman central peak. This allowed one to connect the lone-pair stereochemical activity with octahedral tilting instabilities.[62]

Here, it is shown that experimental GIWAXS data on thin films of $CsPbBr_3$ could reliably be reproduced by *ab initio* molecular dynamics (AIMD) simulations. In this way, it could be demonstrated that the tetragonal phase does not exist on the local scale. By subsequently analyzing the Pb–Br–Pb angles, it is pointed out that, although macroscopically a cubic structure is measured, microscopically the structure stays in its orthorhombic phase at high temperatures. This observation was further supported by a good correspondence between experimental and theoretical Raman spectra, which allowed for a unique assignation of the origin of the Raman active vibrations. Furthermore, the temperature dependence of the Raman bands and their anharmonicity was assessed, giving an insight into the lattice dynamics of $CsPbBr_3$.

II. METHODS

A. GIWAXS

To probe the evolution of the crystal structure with temperature, temperature-dependent synchrotron-based GIWAXS data of a $CsPbBr_3$ thin film were collected at the European Synchrotron Radiation Facility (ESRF) BM26 using the PILATUS@SNBL diffractometer. The monochromatic beam (λ = 1.033 Å) and the parameters of the detector were calibrated on Al_2O_3. The obtained calibrations were implemented in Bubble for further azimuthal integration of 2D images. Data have been recorded during the cooling cycle (temperature range: 473–83 K; ramp rate: 10 K/min). Due to the low-energy barrier involved between the different octahedral tilts, i.e., from cubic to tetragonal, this cooling ramp was confirmed to align with a near equilibrium state for each temperature measured and did not introduce any kinetic effects or thermal hysteresis (in the form of T-dependent structural parameters).

B. Raman spectroscopy

The Raman measurements were carried out using a T64000 Jobin-Yvon Horiba spectrometer equipped with a double monochromator, with a wavelength of 676.4 nm (Krypton laser) as an excitation light source. The sample is optically transparent at this wavelength and no laser heating effect is anticipated. We used a long working distance ×40 objective with a numerical aperture of 0.4 and selected a laser power <5 mW. With an accumulation time of 200 s, the Raman intensity is typically about 5000 counts. The sample temperature was controlled using a liquid nitrogen PI microcryostat adjusting the temperature from 80 to 500 K by a step of 20 K.

C. Computational details

DFT calculations were performed at the PBE-D3(BJ) level of theory.[64–66] The Vienna *Ab initio* Simulation Package (VASP)[67–69] was employed to perform static DFT calculations. Using the projector-augmented wave (PAW) method,[70] a plane wave cut-off of 600 eV was selected, the precision was set to "accurate", and the self-consistent field (SCF) cycle convergence threshold on the electronic energy was 10^{-8} eV. For the α, β, and γ phases, Monkhorst–Pack k-meshes of, respectively, $6 \times 6 \times 6$, $4 \times 4 \times 6$, and $4 \times 4 \times 3$ were applied.[71] Initially, the unit cells of the α, β, and γ phases were geometrically optimized. For that purpose, a set of fixed volume optimizations around the expected equilibrium volume were executed with a convergence threshold on the electronic energy of 10^{-7} eV and, subsequently, a Rose–Vinet fit was constructed to determine the actual equilibrium volume.[72] A final fixed volume optimization was performed at this equilibrium volume. The corresponding Hessian was determined via finite differences of the forces with respect to the atomic displacements. A normal mode analysis yielded the phonon modes in the Γ point. Raman intensities of these phonon modes were determined following a procedure already reported in a previous work.[73] Phonon band structures were generated using Phonopy software,[74] which relied on finite difference calculations of $4 \times 4 \times 4$, $3 \times 3 \times 4$, and $3 \times 3 \times 2$ supercells of, respectively, the α, β, and γ phases in the Γ point.

CP2K with its Quickstep module was applied to run *ab initio* molecular dynamics simulations.[75] These used a Gaussian and plane wave basis set[76] with 1000 Ry as the plane wave cutoff, 60 Ry as the relative cutoff, a TZVP MOLOPT basis set[77] as the atomic basis set, and GTH pseudopotentials.[78] After an equilibration time of 20 ps, MD trajectories with a total length of 80 ps were calculated with a time step of 2 fs. Simulations in the NPT ensemble have been performed on the α and γ phases starting from, respectively, $4 \times 4 \times 4$ and $3 \times 3 \times 2$ supercells of the statically optimized structures. Simulations in the NVT ensemble have been performed on the α, β, and γ phases starting from, respectively, $4 \times 4 \times 4$, $3 \times 3 \times 4$, and $3 \times 3 \times 2$ supercells of the statically optimized structures. In both the NVT and NPT runs, the temperature was controlled using a chain of five Nosé–Hoover thermostats with a time constant of 100 fs.[79] The pressure in the NPT run was controlled at 1 bar with a MTK barostat with a time constant of 1 ps.[80]

Anharmonic frequencies of the normal modes in the Γ point were determined following the procedure proposed by Zhang *et al.*,[81] which has already been successfully applied on lead halide perovskites.[42,44] First, the atomic velocities along the MD run in the NVT ensemble were projected on the normal mode eigenvectors obtained via static DFT. Subsequently, the power spectra of each normal mode were obtained by taking the Fourier transform of the autocorrelation function of the projected velocities. Finally, the anharmonic frequency of the normal mode was obtained after fitting a Lorentzian to its power spectrum.

Dynamic Raman spectra were calculated by taking the discrete Fourier transforms of specific autocorrelation function of the polarizability tensor.[82] Consequently, the polarizability tensor was determined every 10 fs via a finite difference scheme based on the difference between the dipole moments with and without an electric field.[82]

The PXRD patterns were calculated employing the *gpxrdpy* Python package,[83] based on the *pyobjcryst* package and the ObjCryst++ Object-Oriented Crystallographic Library.[84] In accordance with the experiment, the wavelength was set at 1.033 Å. The peak shape was calculated using a pseudo-Voigt shape function with default parameters in *gpxrdpy*. Average PXRD patterns of an MD trajectory were obtained by taking 500 equally distributed snapshots, which proved to give converged results (see Fig. S2 in the supplementary material).

III. RESULTS AND DISCUSSION

A. X-ray diffraction

The temperature dependence of the crystal structure of $CsPbBr_3$ was experimentally investigated through GIWAXS. The resulting scattering data in the temperature range 473–83 K are given in Figs. 2(a) and 2(b) (see also Fig. S1 in the supplementary material) and are fully consistent with earlier x-ray diffraction (XRD) measurements.[49,85,86] At high temperatures, the GIWAXS data contain a limited number of scattering peaks, indicating that the structure is in the highly symmetric α phase. By decreasing the temperature, peak splitting is observed around 403 K. In the literature, this corresponds to the α–β transition.[49] Additional peak splitting is noticed around 358 K, indicating a second phase transition from β to γ, which is also in agreement with previous reports.[49] At low temperatures, the γ phase is still present evidenced by the large number of low-intensity peaks.

In order to gain microscopic insight into the structural changes of $CsPbBr_3$ as a function of temperature, we performed AIMD simulations at 100, 200, 300, 400, and 500 K. These simulations were conducted in the NPT ensemble at a constant pressure of 1 bar to allow for fluctuations in the cell parameters. Starting from a supercell structure of the statically optimized γ phase and after sufficient equilibration, converged powder XRD (PXRD) patterns are obtained in close correspondence with the experimentally determined GIWAXS data [see Fig. 2(d)]. To assign the theoretical PXRD patterns to a specific phase, they are compared with the PXRD patterns of the statically optimized α, β, and γ phases by means of a similarity index.[83] This analysis confirms the presence of the γ phase at 100 K. At higher temperatures, the similarity indices of the α and γ phases yield very similar results, i.e., both take values between 83% and 87% (see Table S2 in the supplementary material). Moreover, when analyzing the similarity indices of PXRD patterns of the snapshots with those of the ideal phases, the chance of having a snapshot leading to the α phase is between 40% and 60%, while the same is true for the γ phase (see Fig. S6 in the supplementary material). Hence, based on the similarity index obtained from the current AIMD simulations, no explicit distinction between the α and γ phase can be made. The fact that the average PXRD patterns at high temperatures do not point to the α phase is most probably due to the limited size of the simulated structure. If $CsPbBr_3$ is microscopically in its γ phase, taking the average over only a small supercell might still contain traces of this phase. In that case, the similarity index will systematically increase toward the α phase above the phase-transition temperature when increasingly larger supercells are considered. However, the simulation of larger supercells was not possible at the current DFT level because of the large computational cost.

Disregarding the supercell size, it is clear, however, that the β phase, apart from a handful of snapshots at 300 and 400 K, does not show up, in contrast to what is claimed in the literature.[49] Based on our theoretical PXRD patterns, the presence of the β phase is marked by the splitting of several low-angle diffraction peaks such as the one due to diffraction in the [100] direction of the α phase at 2θ values of 10° [see Fig. 2(c)]. The splitting of the latter diffraction peak occurs because the distance between neighboring Pb atoms shortens in two of the Cartesian directions due to in-phase tilting of the octahedra, whereas it stays almost unaltered in the remaining Cartesian direction. Consequently, the lack of this splitting in the experimental GIWAXS data suggests that the observed phase does not correspond with the β phase as shown in Fig. 2. The apparent manifestation of a tetragonal phase in terms of lattice vectors as reported by Stoumpos *et al.* is, therefore, most probably the result of averaging over long length and time scales.

In summary, a close correspondence is found between experimental GIWAXS and theoretical PXRD patterns. The latter indicates that the β phase does not exist, at least not on the microscopic scale. They do exhibit an increasing similarity with the α phase at high temperatures, but also, the similarity with the γ phase remains equally high. Based on the presented PXRD patterns, it could not be made out whether this similarity with the α phase is the result of macroscopic averaging or the expression of a truly cubic phase on the local scale.

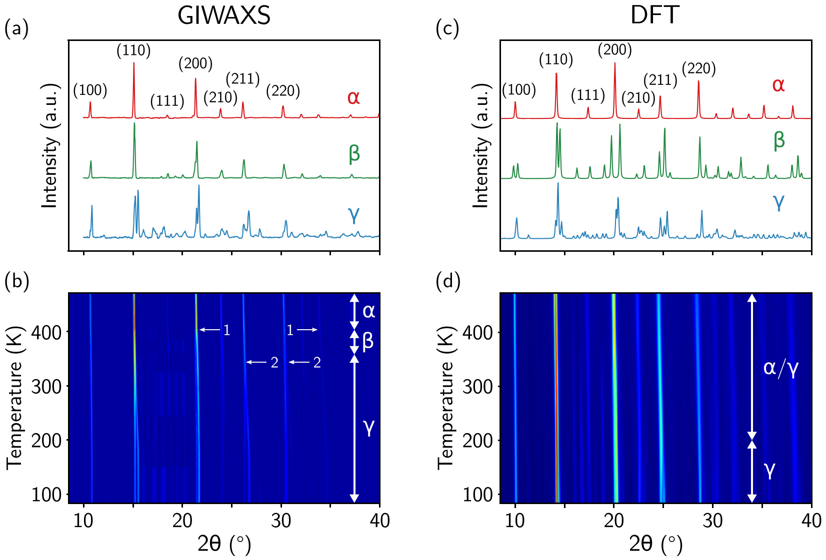

FIG. 2. Temperature-dependent GIWAXS and PXRD patterns (λ = 1.033 Å) of $CsPbBr_3$. (a) and (b) Experimental GIWAXS recorded during the cooling cycle from 473 to 83 K with ramp rate 10 K/min. (a) Integrated profiles of GIWAXS data at 473, 382, and 83 K where, respectively, the α-, β-, and γ-phase are observed. The scattering planes in the α-phase leading to diffraction peaks are indicated. (b) GIWAXS 2θ-temperature profile of the $CsPbBr_3$ thin film through the high-temperature cubic phase (α-phase) to the low-temperature orthorhombic phase (γ-phase) via the intermediate tetragonal phase (β-phase). Arrows 1 and 2 indicate the position of the peak splitting corresponding to the phase transition from the α- to β-phase and from the β- to γ-phase, respectively. (c) and (d) Theoretical PXRD patterns. (c) Normalized PXRD patterns obtained from a single snapshot of the statically optimized α-, β-, and γ-phases. The scattering planes in the α-phase leading to diffraction peaks are indicated. (d) PXRD 2θ-temperature profile of $CsPbBr_3$ obtained through averaging of MD simulations in the NPT ensemble at 100, 200, 300, 400, and 500 K.

To deal with this remaining question, it is instructive to analyze the evolution of local structural parameters such as the Pb–Br–Pb angle between Pb atoms of neighboring octahedra and the connecting Br atom [see inset in Fig. 3(a)].[87] This parameter can be easily extracted from the snapshots of the MD simulations, and its distribution as a function of temperature is shown in Fig. 3(a) for simulations on a supercell of the statically optimized γ phase. At low temperatures, this distribution is strongly peaked between 150° and 160°, indicating that all the Pb–Br–Pb angles are tilted and, consequently, that the structure is microscopically in its γ phase. By increasing the temperature, the distribution of the Pb–Br–Pb angles broadens and shifts slightly to higher angles. However, even at 500 K, there exist almost no angles around 180°, corresponding to an untilted situation. More than that, the distribution strongly decreases when approaching 180°, where it eventually reaches a negligible probability, mainly due to the significantly reduced number of configurations exhibiting angles around 180°. This indicates that an untilted situation is highly unlikely. Moreover, the average Pb–Br–Pb angle does not increase by more than 2° when increasing the temperature from 100 to 500 K. This shows that an increase in temperature might increase the variation in the tilting angle, but the average tilting remains more or less unchanged and, hence, even at 500 K, $CsPbBr_3$ is in its γ phase on the local scale.

Interestingly, the aforementioned theoretical picture differs when NPT simulations are performed starting, instead, from a $4 \times 4 \times 4$ supercell of the statically optimized α phase. In this case, the distribution of the Pb–Br–Pb angles [see Fig. 3(c)] is bimodal at 100 K: one peak is present around 150° and another one around 170°. Evidently, due to the discrepancies in the distribution of the tilting angle that affect the structural geometry, the PXRD pattern is different as well. While the PXRD pattern of the NPT simulation starting from the γ phase corresponds with a γ phase diffraction pattern [see Fig. 3(b)], a β phase diffraction pattern emerges when starting from the α phase [see Fig. 3(d)]. When the temperature is increased to 200 K and higher, both the distributions of the Pb–Br–Pb angle and the PXRD patterns strongly resemble the distributions and PXRD patterns obtained previously. Apparently, the deviation between the two sets of NPT simulations is restricted to low temperatures. The reason for the emergence of either γ- or β-phase geometries at low temperatures might be related with the activation of particular tilting modes. Below a certain temperature, the out-of-phase tilting is, in contrast to the in-phase tilting, probably not activated. As such, the α phase can transform to the β phase upon in-phase tilting, but the barrier of out-of-phase tilting leading to the γ phase cannot be overcome. Hence, the structure remains frozen in the β phase, although the γ phase is more stable at this temperature. This is also reflected by the average potential energy during the MD simulations at 100 K, which is, per mole of the crystallographic $CsPbBr_3$ unit, 2.3 kJ higher starting from the α phase than the γ phase. However, this β phase differs from its formal definition shown in Fig. 1, as there are no untilted Pb–Br–Pb angles (180°) along one direction, but rather slightly tilted (170°) ones. Evidently, as before, the untilted configuration remains highly improbable, irrespective of the initial configuration. One can thus argue that the metastable phase that is formed is a kind of γ phase rather than β phase. The presence of different metastable γ phases

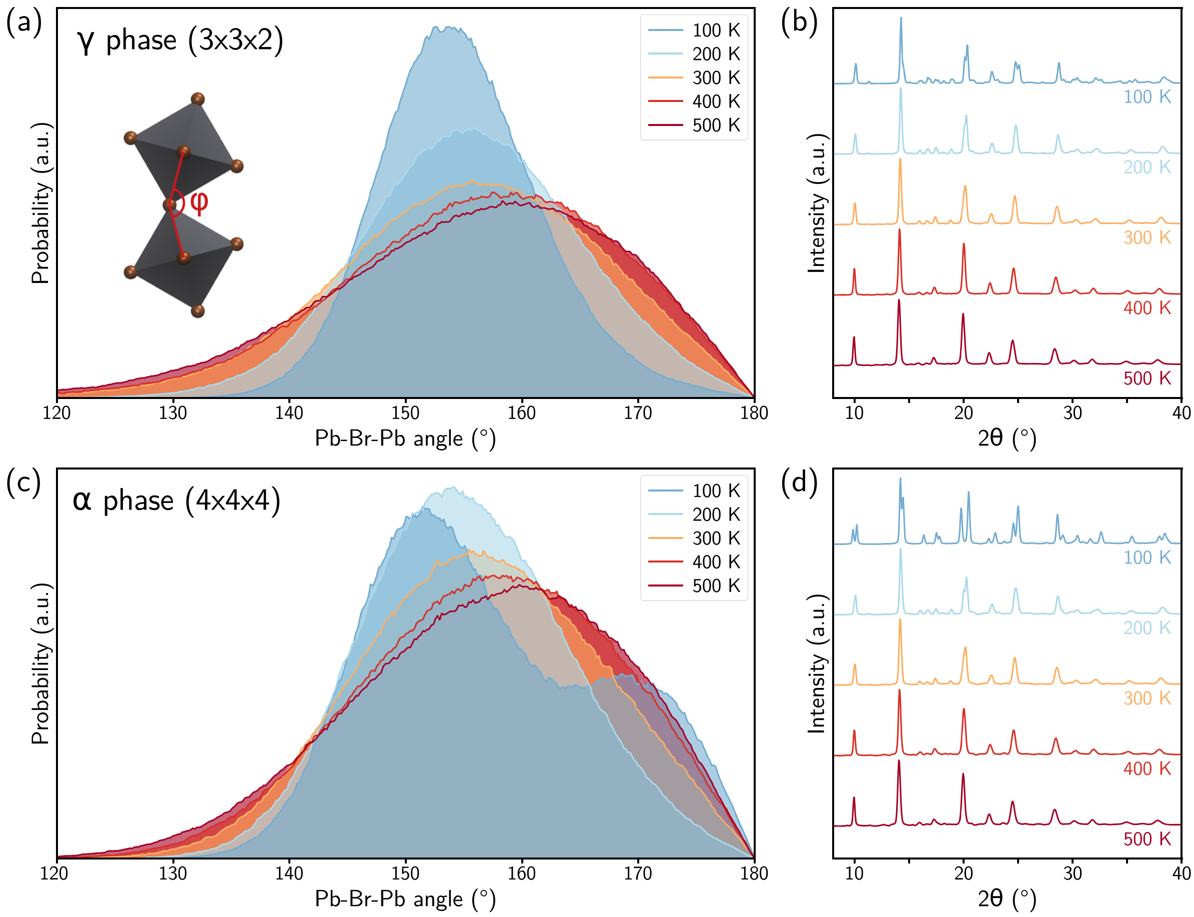

FIG. 3. Distributions of the Pb–Br–Pb angles [(a) and (c)] and average PXRD patterns [(b) and (d)] at different temperatures for MD simulations in the NPT ensemble starting from either a 3 × 3 × 2 supercell of the ideal orthorhombic (γ) phase [(a) and (b)] or a 4 × 4 × 4 supercell of the ideal cubic (α) phase [(c) and (d)]. The Pb–Br–Pb angle is visualized by angle φ.

has recently been pointed out by Braeckevelt *et al.* in $CsPbI_3$[88] and this observation also fits in the theoretical prediction of the multi-well potential.[41]

The above-mentioned discussion demonstrates that the starting conditions of the simulation can affect the theoretical result. When performing simulations on $CsPbBr_3$ at low temperatures, it is important to select a starting configuration that is located closely to the absolute minimum on the potential energy surface in order to sample the correct phase space. When this is not the case, the sampled phase space might get stuck in a metastable phase and the results can deviate from experiments.

B. Raman spectroscopy

To gain an insight into its lattice dynamics, experimental and theoretical Raman spectra have been investigated. The results of temperature-dependent Raman experiments on $CsPbBr_3$ are given in Figs. 4(a) and 4(b) and S17 and are in agreement with reports of Yaffe *et al.*[29] and Guo *et al.*[59] At temperatures below 180 K, sharp and well-resolved Raman spectra are observed, where two prevailing Raman bands below 50 cm^{-1} can be identified, aside from a set of three peaks around 65–85 cm^{-1}, and a broad, low-intensity feature centered around 130 cm^{-1} can be identified. With increasing temperature, all the peaks start to diffuse and undergo a decrease in frequency. The broadening of the bands is caused by thermal vibration of the crystal lattice, electronic involvement, and interactions between participative phonons, whereas the decrease in frequency is due to the temperature-assisted lattice contraction, similarly observed for other semiconductors.[60] At 300 K, only four broad Raman peaks are visible at around 25, 40 cm^{-1} (very weak), 75, and 125 cm^{-1} (very weak). Eventually, one single clear hump is observed at around 70 cm^{-1} in the spectra above 400 K. Additionally, a central (zero-frequency) peak increases in intensity when increasing the temperature. This central peak has been dedicated to the manifestation of local polar thermal fluctuations.[29]

The Raman spectra have been artificially separated in three temperature regions according to the experimentally reported stability regions of the α, β, and γ phases. This separation does not

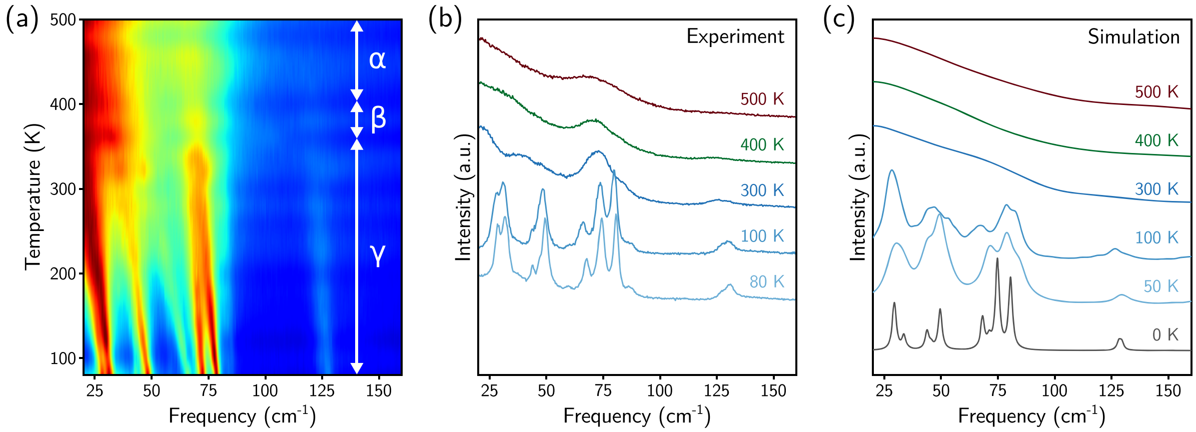

FIG. 4. Temperature-dependent Raman spectra of $CsPbBr_3$. Raman spectra are normalized at each temperature. (a) Color surface plot showing the evolution of the experimental Raman spectra as a function of temperature. The experimentally observed phase transitions are indicated. (b) Experimental Raman spectra at distinct temperatures. Blue curves indicate structures in the γ-phase, green curves indicate structures in the β-phase, and red curves indicate structures in the α-phase. (c) Theoretical Raman spectra obtained from MD simulations in the NVT ensemble at distinct temperatures. They received appropriate scaling factors and Lorentzian broadening. The Raman spectrum at 0 K corresponds to the static DFT result of the γ phase. Experimental and theoretical Raman spectra in (b) and (c) were offset for better visibility. Colors of the curves are based on the experimental stable phase at the respective temperature.

correspond with the microscopic situation, as we have shown previously that only the γ phase is present on the local scale, whereas the β and α phases only appear as macroscopic averages. The Raman spectra at high temperatures provide another argument for this rationale because factor group analysis predicts no Raman activity of the cubic phase.[89] As diffuse Raman spectra and a central peak at 0 cm^{-1} are observed above 400 K, this means that the structure is highly dynamic at local length scales (i.e., a few unit cells), fluctuating among different non-cubic structures in such a way as to appear cubic on average.[29,40,53,54]

To explain the origin of the Raman active vibrations, the contributing phonon modes have been identified and their temperature dependence has been characterized via AIMD simulations. Ideally, the simulations are performed in the NPT ensemble to account for the possible fluctuations in the cell shape. However, the barostat interfered with the lattice dynamics yielding spurious contributions to the velocity power spectrum (VPS) and Raman spectrum, especially at lower temperatures (see Figs. S14, S15, and S18 in the supplementary material). For that purpose, AIMD simulations have been performed in the NVT ensemble, which, on one hand, did not suffer from the interference of a barostat, but, on the other hand, fixed the cell parameters. NVT trajectories starting from supercells of the statically optimized α, β, and γ phases have been generated. Analysis of the Pb–Br–Pb angles showed that simulations on the α and γ phases yielded structures that were locally in the γ phase for all considered temperatures. However, the simulations on the β phase, in agreement with the NPT results on the α phase, yielded metastable β phase structures at 50 and 100 K (see Figs. S12 and S13 in the supplementary material). As it has been evidenced before that $CsPbBr_3$ is locally present in its γ phase, the results presented hereafter originate from NVT simulations run on a supercell of the γ phase. We refer to Section S4 in the supplementary material for the results of the NVT simulations on α-and β-phase structures.

Figure 4(c) shows the Raman spectra determined via AIMD at different temperatures, together with the static DFT Raman spectrum of the γ phase. The dynamic Raman spectra were calculated following the procedure outlined by Thomas *et al.*[82] (see also Sec. II). Moreover, to account for the known mismatch between the actual bond distances and those calculated via DFT, the AIMD spectra were shifted by applying a scaling factor.[90] Furthermore, they also received additional Lorentzian broadening in order to improve the correspondence with the experiment, which inherently contains a certain amount of defects. The original dynamic Raman spectra without scaling and additional broadening are given in Fig. S19 of the supplementary material. The optimal scaling factor was determined by calculating the similarity index between the theoretical and experimental spectrum.[83] At 100 K, this scaling factor was found to be 1.035 in agreement with our earlier work using the same level of theory.[91] The additional Lorentzian shape had a full width at half-maximum (FWHM) of 2 cm^{-1}. The theoretical spectrum at 50 K has been compared with the experimental spectrum at 80 K. As not all Raman active modes show the same temperature dependence (this will be discussed later), the optimal scaling factor and the Lorentzian broadening were slightly larger, i.e., 1.055 and FWHM of 3 cm^{-1}, respectively. At temperatures of 300 K and higher, the scaling factor was fixed at the optimal value at 100 K because the presence of the central peak complicated a unique determination of the optimal scaling factor. The additional Lorentzian broadening was determined to have a FWHM of 16, 19, and 22 cm^{-1} at 300, 400, and 500 K, respectively. Overall, a satisfying agreement between theory and experiment is obtained, evidenced by similarity indices of 92% and higher (see also Table S3 in the supplementary material). Below 100 K, the different Raman bands can clearly be distinguished in both the theoretical and experimental spectra. From 300 K onward, however, only diffuse Raman bands are present in the experimental spectra and, in the theoretical spectra, the distinct Raman bands are barely observable against the central Raman peak, making it difficult to draw conclusions from the high-temperature spectra.

The agreement between experiment and theory, especially at low temperatures, justifies the identification of the Raman active normal modes via DFT calculations. Figure 5(a) directly compares the experimental Raman spectrum at 100 K with the corresponding AIMD result. Four regions of Raman active normal modes can be recognized. The frequency region with the lowest frequencies is characterized by normal modes inducing mainly out-of-plane tilting of the octahedra (modes A and B). A second frequency region contains normal modes inducing an in-plane tilting of the octahedra, possibly combined with slight distortions of the octahedra. A third set of normal modes can be described by distortions of the octahedra in which neighboring Br atoms move toward each other. Finally, the Raman active modes with the highest frequency induce distortions of the octahedra through opposite Br atoms moving toward each other. For each frequency region, a single mode is shown in Fig. 5(c). The normal modes inducing in-phase and out-of-phase tilting of the octahedra typically have the lowest frequencies as this type of motion is almost unhindered, in contrast to normal modes inducing distortions of the octahedra.

The MD approach allowed us to estimate the temperature dependence and anharmonicity of the Raman active normal modes by projecting the velocities on the respective normal modes (see Sec. II). At 50 and 100 K, the VPS of the normal modes resulted in clear Lorentzian line shapes (see Fig. S25), indicating that at these temperatures, the phonon modes behave practically harmonically. At 300 K, the VPS spectra are already substantially broadened, but the mixing of normal modes is limited, still making it possible to obtain reliable fits of the Lorentzian line shapes. Increasing the temperature even more enhances the occurrence of mode mixing, pointing out that anharmonic effects are becoming increasingly dominant. Therefore, fitting a Lorentzian line shape to the VPS spectra of the normal modes is no longer meaningful, and the discussion of the temperature dependence of the theoretical Raman frequencies is restricted to the temperature range 50–300 K. Figure 5(b) shows

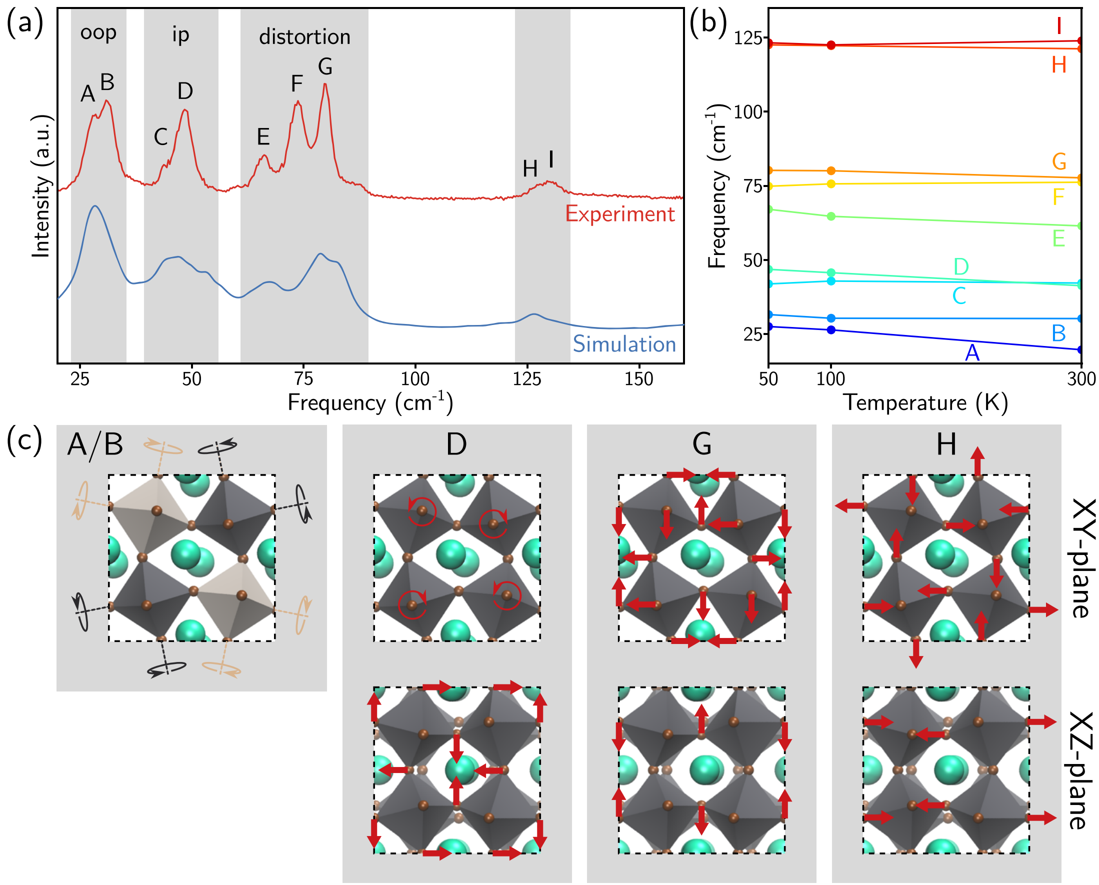

FIG. 5. (a) Comparison of the experimental and theoretical Raman spectra of $CsPbBr_3$ at 100 K. The most intense Raman peaks are highlighted. (b) Predicted temperature dependence of the vibrational frequencies of the Raman bands. (c) Visualization of Raman active normal modes: (A/B) out-of-phase (oop) tilting of the octahedra, (D) in-phase (ip) tilting combined with distortion of the octahedra, (G) distortion of octahedra via neighboring Br atoms moving toward each other, and (H) distortion of octahedra via opposite Br atoms moving toward each other. A visualization of the other highlighted modes can be found in the supplementary material. Almost all modes are accompanied by rattling of the Cs atoms (not shown in the figure).

a clear monotonous decrease of the vibrational frequency as a function of temperature for modes A, D, and E. The other Raman active modes have a frequency that does not differ by more than 2 cm^{-1} as a function of temperature. The strong frequency decrease of the three specific Raman bands is in agreement with observations within the experimental Raman spectrum [see Fig. 4(a)]. However, in the experiment, other Raman active modes, in particular, modes F, G, H, and I, do also show a slight decrease in frequency when the temperature is increased, which is not observed in the simulations. This might be a result of the limitations of the NVT ensemble, keeping cell parameters fixed and not allowing for temperature-assisted lattice contraction. In general, simulations with fixed unit cell parameters need to be interpreted with care due to their limitations to account for complex multi-phonon scattering. On a final note, our analysis shows that, although there is a decrease in frequency upon increasing temperature, the normal modes in CsPbBr_3 never become very soft. This confirms that possible phase transitions within CsPbBr_3 are not displacive, supporting the rationalization that they do not exist at all.

IV. CONCLUSIONS

In this combined experimental and theoretical study, the apparent phase transitions in CsPbBr_3 as a function of temperature have been fully elucidated. Temperature-dependent GIWAXS measurements showed sudden peak splitting in the scattering data around 358 and 403 K, corresponding to phase transitions between the γ and β phases and between the β and α phases, respectively, in agreement with the literature. Theoretical simulations of the PXRD patterns were able to correctly predict the GIWAXS data. Subsequent analysis of the simulated PXRD patterns revealed that the α and β phases do not exist on the local scale, but, due to dynamic disorder, appear as averages over longer time and length scales. In-depth investigation of the structural parameters made clear that all Pb–Br–Pb angles remain tilted under all conditions with an average tilt angle between 150° and 160°, demonstrating that CsPbBr_3 is locally always in its γ phase.

In addition to the crystal structure, the lattice dynamics of CsPbBr_3 as a function of temperature was also investigated via Raman spectroscopy. A sound agreement was obtained between theoretical Raman spectra of the γ phase and experiment. At low temperatures, the clear experimental Raman bands could be reliably simulated, whereas, at high temperatures, the presence of the central peak, due to local polar fluctuations, rendered a meaningful comparison difficult. Analysis of the Raman spectra delineated four distinct regions of Raman active vibrations. The two frequency regions with the lowest frequencies could be characterized by phonon modes inducing out-of-phase and in-phase tilting of the octahedra, respectively. The other two regions with a higher frequency contained phonon modes inducing distortions of the octahedra. Some of these phonon modes showed a significant decrease in frequency as a function of temperature, which was also correctly predicted by theory.

Our extensive structural and vibrational characterization yields an important insight into the stability and dynamics of CsPbBr_3 on the microscopic scale, an insight that is likely transferable to other MHPs for an increased understanding of their properties.

SUPPLEMENTARY MATERIAL

See the supplementary material for temperature-dependent GIWAXS data, theoretical PXRD patterns, distribution of Pb–Br–Pb angles, velocity power spectra, temperature-dependent experimental Raman spectra, theoretical Raman spectra, visualization of Raman active normal modes, and VPS of velocities projected on the normal modes.

ACKNOWLEDGMENTS

The authors gratefully acknowledge financial support from the Research Foundation—Flanders (FWO Grant Nos. 1SC1319N, G098319N, S002019N “PROCEED,” and S004322N “GIGAPIXEL”), the Research Fund of Ghent University (Grant No. iBOF-21-085 PERSIST), the KU Leuven Research Fund (Grant No. iBOF-21-085 PERSIST), and the Flemish government through long-term structural funding Methusalem (CASAS2, Meth/15/04). V.V.S. further acknowledges the Research Fund of Ghent University (BOF) for its financial support. P.P. was supported by the OPEP project originating from EUR Grant NanoX No. ANR-17-EURE-0009 in the framework of the French PIA. The computational resources and services used in this work were provided by the Flemish Supercomputer Center (VSC), funded by the Research Foundation—Flanders (FWO) and the Flemish Government.

AUTHOR DECLARATIONS

Conflict of Interest

The authors have no conflicts to disclose.

Author Contributions

Alexander E. J. Hoffman: Conceptualization (equal); Data curation (equal); Formal analysis (equal); Investigation (equal); Methodology (equal); Software (equal); Validation (equal); Visualization (equal); Writing – original draft (equal). **Rafikul Ali Saha**: Data curation (equal); Formal analysis (equal); Investigation (equal); Methodology (equal). **Sander Borgmans**: Data curation (equal); Formal analysis (equal); Investigation (equal); Methodology (equal); Writing – review & editing (equal). **Pascal Puech**: Data curation (equal); Formal analysis (equal); Investigation (equal); Methodology (equal); Writing – review & editing (equal). **Tom Braeckevelt**: Conceptualization (equal); Investigation (equal); Methodology (equal); Writing – review & editing (equal). **Maarten B. J. Roeffaers**: Conceptualization (equal); Funding acquisition (equal); Investigation (equal); Methodology (equal); Project administration (equal); Resources (equal); Supervision (equal); Writing – review & editing (equal). **Julian A. Steele**: Conceptualization (equal); Data curation (equal); Formal analysis (equal); Investigation (equal); Methodology (equal); Validation (equal); Writing – review & editing (equal). **Johan Hofkens**: Conceptualization (equal); Formal analysis (equal); Funding acquisition (equal); Investigation (equal); Methodology (equal); Project administration (equal); Resources (equal); Supervision (equal); Validation (equal); Writing – review & editing (equal). **Veronique Van Speybroeck**: Conceptualization (equal); Formal analysis (equal); Funding acquisition (equal); Investigation (equal); Methodology (equal); Project administration (equal); Resources (equal); Software (equal); Supervision (equal); Validation (equal); Writing – review & editing (equal).

DATA AVAILABILITY

The data that support the findings of this study are available within the article and its supplementary material. All structure files and input scripts used to obtain the results are available from the online GitHub repository at https://github.com/AlexanderHoffman/supporting-info.

REFERENCES

[1] M. A. Green, A. Ho-Baillie, and H. J. Snaith, "The emergence of perovskite solar cells," Nat. Photonics **8**, 506–514 (2014).

[2] J.-P. Correa-Baena, M. Saliba, T. Buonassisi, M. Grätzel, A. Abate, W. Tress, and A. Hagfeldt, "Promises and challenges of perovskite solar cells," Science **358**, 739–744 (2017).

[3] S. I. Seok, M. Grätzel, and N.-G. Park, "Methodologies toward highly efficient perovskite solar cells," Small **14**, 1704177 (2018).

[4] J. Y. Kim, J.-W. Lee, H. S. Jung, H. Shin, and N.-G. Park, "High-efficiency perovskite solar cells," Chem. Rev. **120**, 7867–7918 (2020).

[5] R. Pandey, G. Vats, J. Yun, C. R. Bowen, A. W. Y. Ho-Baillie, J. Seidel, K. T. Butler, and S. I. Seok, "Mutual insight on ferroelectrics and hybrid halide perovskites: A platform for future multifunctional energy conversion," Adv. Mater. **31**, 1807376 (2019).

[6] A. Kojima, K. Teshima, Y. Shirai, and T. Miyasaka, "Organometal halide perovskites as visible-light sensitizers for photovoltaic cells," J. Am. Chem. Soc. **131**, 6050–6051 (2009).

[7] J. Jeong, M. Kim, J. Seo, H. Lu, P. Ahlawat, A. Mishra, Y. Yang, M. A. Hope, F. T. Eickemeyer, M. Kim, Y. J. Yoon, I. W. Choi, B. P. Darwich, S. J. Choi, Y. Jo, J. H. Lee, B. Walker, S. M. Zakeeruddin, L. Emsley, U. Rothlisberger, A. Hagfeldt, D. S. Kim, M. Grätzel, and J. Y. Kim, "Pseudo-halide anion engineering for α-FAPbI3 perovskite solar cells," Nature **592**, 381–385 (2021).

[8] M. Green, E. Dunlop, J. Hohl-Ebinger, M. Yoshita, N. Kopidakis, and X. Hao, "Solar cell efficiency tables (version 57)," Prog. Photovolt.: Res. Appl. **29**, 3–15 (2021).

[9] T. Leijtens, G. E. Eperon, N. K. Noel, S. N. Habisreutinger, A. Petrozza, and H. J. Snaith, "Stability of metal halide perovskite solar cells," Adv. Energy Mater. **5**, 1500963 (2015).

[10] S. Adjokatse, H.-H. Fang, and M. A. Loi, "Broadly tunable metal halide perovskites for solid-state light-emission applications," Mater. Today **20**, 413–424 (2017).

[11] Y. Wang, M.-L. Gao, J.-L. Wu, and X.-W. Zhang, "Metal halide perovskite photodetectors: Material features and device engineering," Chin. Phys. B **28**, 018502 (2019).

[12] H. Zhu, A. Liu, and Y.-Y. Noh, "Recent progress on metal halide perovskite field-effect transistors," J. Inf. Disp. **22**, 257–268 (2021).

[13] X.-K. Liu, W. Xu, S. Bai, Y. Jin, J. Wang, R. H. Friend, and F. Gao, "Metal halide perovskites for light-emitting diodes," Nat. Mater. **20**, 10–21 (2021).

[14] L. Meng, J. You, and Y. Yang, "Addressing the stability issue of perovskite solar cells for commercial applications," Nat. Commun. **9**, 1–4 (2018).

[15] J. S. Manser, M. I. Saidaminov, J. A. Christians, O. M. Bakr, and P. V. Kamat, "Making and breaking of lead halide perovskites," Acc. Chem. Res. **49**, 330–338 (2016).

[16] C. C. Boyd, R. Cheacharoen, T. Leijtens, and M. D. McGehee, "Understanding degradation mechanisms and improving stability of perovskite photovoltaics," Chem. Rev. **119**, 3418–3451 (2018).

[17] Z. Zhu, Q. Sun, Z. Zhang, J. Dai, G. Xing, S. Li, X. Huang, and W. Huang, "Metal halide perovskites: Stability and sensing-ability," J. Mater. Chem. C **6**, 10121–10137 (2018).

[18] R. Wang, M. Mujahid, Y. Duan, Z. K. Wang, J. Xue, and Y. Yang, "A review of perovskites solar cell stability," Adv. Funct. Mater. **29**, 1808843 (2019).

[19] C. C. Stoumpos, C. D. Malliakas, and M. G. Kanatzidis, "Semiconducting tin and lead iodide perovskites with organic cations: Phase transitions, high mobilities, and near-infrared photoluminescent properties," Inorg. Chem. **52**, 9019–9038 (2013).

[20] M. R. Filip, G. E. Eperon, H. J. Snaith, and F. Giustino, "Steric engineering of metal-halide perovskites with tunable optical band gaps," Nat. Commun. **5**, 5757 (2014).

[21] A. Osherov, E. M. Hutter, K. Galkowski, R. Brenes, D. K. Maude, R. J. Nicholas, P. Plochocka, V. Bulović, T. J. Savenije, and S. D. Stranks, "The impact of phase retention on the structural and optoelectronic properties of metal halide perovskites," Adv. Mater. **28**, 10757–10763 (2016).

[22] C. Katan, A. D. Mohite, and J. Even, "Entropy in halide perovskites," Nat. Mater. **17**, 377–379 (2018).

[23] C. E. Patrick, K. W. Jacobsen, and K. S. Thygesen, "Anharmonic stabilization and band gap renormalization in the perovskite $\mathrm{CsSnI_3}$," Phys. Rev. B **92**, 201205 (2015).

[24] E. L. Da Silva, J. M. Skelton, S. C. Parker, and A. Walsh, "Phase stability and transformations in the halide perovskite $\mathrm{CsSnI_3}$," Phys. Rev. B **91**, 144107 (2015).

[25] I. P. Swainson, C. Stock, S. F. Parker, L. Van Eijck, M. Russina, and J. W. Taylor, "From soft harmonic phonons to fast relaxational dynamics in $\mathrm{CH_3NH_3PbBr_3}$," Phys. Rev. B **92**, 100303 (2015).

[26] L. D. Whalley, J. M. Skelton, J. M. Frost, and A. Walsh, "Phonon anharmonicity, lifetimes, and thermal transport in $\mathrm{CH_3NH_3PbI_3}$ from many-body perturbation theory," Phys. Rev. B **94**, 220301 (2016).

[27] J. Even, M. Carignano, and C. Katan, "Molecular disorder and translation/rotation coupling in the plastic crystal phase of hybrid perovskites," Nanoscale **8**, 6222–6236 (2016).

[28] C. La-o-vorakiat, H. Xia, J. Kadro, T. Salim, D. Zhao, T. Ahmed, Y. M. Lam, J.-X. Zhu, R. A. Marcus, M.-E. Michel-Beyerle, and E. E. M. Chia, "Phonon mode transformation across the orthohombic–tetragonal phase transition in a lead iodide perovskite $\mathrm{CH_3NH_3PbI_3}$: A terahertz time-domain spectroscopy approach," J. Phys. Chem. Lett. **7**, 1–6 (2016).

[29] O. Yaffe, Y. Guo, L. Z. Tan, D. A. Egger, T. Hull, C. C. Stoumpos, F. Zheng, T. F. Heinz, L. Kronik, M. G. Kanatzidis, J. S. Owen, A. M. Rappe, M. A. Pimenta, and L. E. Brus, "Local polar fluctuations in lead halide perovskite crystals," Phys. Rev. Lett. **118**, 136001 (2017).

[30] Y. Guo, O. Yaffe, T. D. Hull, J. S. Owen, D. R. Reichman, and L. E. Brus, "Dynamic emission Stokes shift and liquid-like dielectric solvation of band edge carriers in lead-halide perovskites," Nat. Commun. **10**, 1–8 (2019).

[31] M. Songvilay, N. Giles-Donovan, M. Bari, Z.-G. Ye, J. L. Minns, M. A. Green, G. Xu, P. M. Gehring, K. Schmalzl, W. D. Ratcliff, C. M. Brown, D. Chernyshov, W. van Beek, S. Cochran, and C. Stock, "Common acoustic phonon lifetimes in inorganic and hybrid lead halide perovskites," Phys. Rev. Mater. **3**, 093602 (2019).

[32] R. Sharma, Z. Dai, L. Gao, T. M. Brenner, L. Yadgarov, J. Zhang, Y. Rakita, R. Korobko, A. M. Rappe, and O. Yaffe, "Elucidating the atomistic origin of anharmonicity in tetragonal $\mathrm{CH_3NH_3PbI_3}$ with Raman scattering," Phys. Rev. Mater. **4**, 092401 (2020).

[33] X. Wang, K. Patel, S. Prosandeev, Y. Zhang, C. Zhong, B. Xu, and L. Bellaiche, "Finite-temperature dynamics in cesium lead iodide halide perovskite," Adv. Funct. Mater. **31**, 2106264 (2021).

[34] T. Lanigan-Atkins, X. He, M. J. Krogstad, D. M. Pajerowski, D. L. Abernathy, G. N. M. N. Xu, Z. Xu, D.-Y. Chung, M. G. Kanatzidis, S. Rosenkranz, R. Osborn, and O. Delaire, "Two-dimensional overdamped fluctuations of the soft perovskite lattice in $\mathrm{CsPbBr_3}$," Nat. Mater. **20**, 977–983 (2021).

[35] F. Brivio, J. M. Frost, J. M. Skelton, A. J. Jackson, O. J. Weber, M. T. Weller, A. R. Goñi, A. M. A. Leguy, P. R. F. Barnes, and A. Walsh, "Lattice dynamics and vibrational spectra of the orthorhombic, tetragonal, and cubic phases of methylammonium lead iodide," Phys. Rev. B **92**, 144308 (2015).

[36] P. Guo, Y. Xia, J. Gong, C. C. Stoumpos, K. M. McCall, G. C. B. Alexander, Z. Ma, H. Zhou, D. J. Gosztola, J. B. Ketterson, M. G. Kanatzidis, T. Xu, M. K. Y. Chan, and R. D. Schaller, "Polar fluctuations in metal halide perovskites uncovered by acoustic phonon anomalies," ACS Energy Lett. **2**, 2463–2469 (2017).

[37] R. X. Yang, J. M. Skelton, E. L. Da Silva, J. M. Frost, and A. Walsh, "Spontaneous octahedral tilting in the cubic inorganic cesium halide perovskites $CsSnX_3$ and $CsPbX_3$ (X = F, Cl, Br, I)," J. Phys. Chem. Lett. **8**, 4720–4726 (2017).

[38] A. Marronnier, H. Lee, B. Geffroy, J. Even, Y. Bonnassieux, and G. Roma, "Structural instabilities related to highly anharmonic phonons in halide perovskites," J. Phys. Chem. Lett. **8**, 2659–2665 (2017).

[39] A. Marronnier, G. Roma, S. Boyer-Richard, L. Pedesseau, J.-M. Jancu, Y. Bonnassieux, C. Katan, C. C. Stoumpos, M. G. Kanatzidis, and J. Even, "Anharmonicity and disorder in the black phases of cesium lead iodide used for stable inorganic perovskite solar cells," ACS Nano **12**, 3477–3486 (2018).

[40] S. McKechnie, J. M. Frost, D. Pashov, P. Azarhoosh, A. Walsh, and M. Van Schilfgaarde, "Dynamic symmetry breaking and spin splitting in metal halide perovskites," Phys. Rev. B **98**, 085108 (2018).

[41] J. Klarbring, "Low-energy paths for octahedral tilting in inorganic halide perovskites," Phys. Rev. B **99**, 104105 (2019).

[42] H.-Y. Gu, W.-J. Yin, and X.-G. Gong, "Significant phonon anharmonicity drives phase transitions in $CsPbI_3$," Appl. Phys. Lett. **119**, 191101 (2021).

[43] R. Ben Sadok, D. Hammoutène, and N. Plugaru, "New phase transitions driven by soft phonon modes for CsPbBr3: Density functional theory study," Phys. Status Solidi B **258**, 2000289 (2021).

[44] J. Lahnsteiner and M. Bokdam, "Anharmonic lattice dynamics in large thermodynamic ensembles with machine-learning force fields: $CsPbBr_3$, a phonon liquid with Cs rattlers," Phys. Rev. B **105**, 024302 (2022).

[45] J. Liang, C. Wang, Y. Wang, Z. Xu, Z. Lu, Y. Ma, H. Zhu, Y. Hu, C. Xiao, X. Yi, G. Zhu, H. Lv, L. Ma, T. Chen, Z. Tie, Z. Jin, and J. Liu, "All-inorganic perovskite solar cells," J. Am. Chem. Soc. **138**, 15829–15832 (2016).

[46] G. E. Eperon, G. M. Paternò, R. J. Sutton, A. Zampetti, A. A. Haghighirad, F. Cacialli, and H. J. Snaith, "Inorganic caesium lead iodide perovskite solar cells," J. Mater. Chem. A **3**, 19688–19695 (2015).

[47] R. J. Sutton, M. R. Filip, A. A. Haghighirad, N. Sakai, B. Wenger, F. Giustino, and H. J. Snaith, "Cubic or orthorhombic? Revealing the crystal structure of metastable black-phase $CsPbI_3$ by theory and experiment," ACS Energy Lett. **3**, 1787–1794 (2018).

[48] J. A. Steele, H. Jin, I. Dovgaliuk, R. F. Berger, T. Braeckevelt, H. Yuan, C. Martin, E. Solano, K. Lejaeghere, S. M. J. Rogge, C. Notebaert, W. Vandezande, K. P. F. Janssen, B. Goderis, E. Debroye, Y.-K. Wang, Y. Dong, D. Ma, M. Saidaminov, H. Tan, Z. Lu, V. Dyadkin, D. Chernyshov, V. Van Speybroeck, E. H. Sargent, J. Hofkens, and M. B. J. Roeffaers, "Thermal unequilibrium of strained black $CsPbI_3$ thin films," Science **365**, 679–684 (2019).

[49] C. C. Stoumpos, C. D. Malliakas, J. A. Peters, Z. Liu, M. Sebastian, J. Im, T. C. Chasapis, A. C. Wibowo, D. Y. Chung, A. J. Freeman, B. W. Wessels, and M. G. Kanatzidis, "Crystal growth of the perovskite semiconductor $CsPbBr_3$: A new material for high-energy radiation detection," Cryst. Growth Des. **13**, 2722–2727 (2013).

[50] I. Pallikara, P. Kayastha, J. M. Skelton, and L. D. Whalley, "The physical significance of imaginary phonon modes in crystals," Electron. Struct. **4**, 033002 (2022).

[51] R. A. Cowley, "Temperature dependence of a transverse optic mode in strontium titanate," Phys. Rev. Lett. **9**, 159 (1962).

[52] A. Cohen, T. M. Brenner, J. Klarbring, R. Sharma, D. H. Fabini, R. Korobko, P. K. Nayak, O. Hellman, and O. Yaffe, "Diverging expressions of anharmonicity in halide perovskites," Adv. Mater. **34**, 2107932 (2022).

[53] C. Quarti, E. Mosconi, J. M. Ball, V. D'Innocenzo, C. Tao, S. Pathak, H. J. Snaith, A. Petrozza, and F. De Angelis, "Structural and optical properties of methylammonium lead iodide across the tetragonal to cubic phase transition: Implications for perovskite solar cells," Energy Environ. Sci. **9**, 155–163 (2016).

[54] A. N. Beecher, O. E. Semonin, J. M. Skelton, J. M. Frost, M. W. Terban, H. Zhai, A. Alatas, J. S. Owen, A. Walsh, and S. J. L. Billinge, "Direct observation of dynamic symmetry breaking above room temperature in methylammonium lead iodide perovskite," ACS Energy Lett. **1**, 880–887 (2016).

[55] F. Bertolotti, L. Protesescu, M. V. Kovalenko, S. Yakunin, A. Cervellino, S. J. L. Billinge, M. W. Terban, J. S. Pedersen, N. Masciocchi, and A. Guagliardi, "Coherent nanotwins and dynamic disorder in cesium lead halide perovskite nanocrystals," ACS Nano **11**, 3819–3831 (2017).

[56] M. A. Carignano, S. A. Aravindh, I. S. Roqan, J. Even, and C. Katan, "Critical fluctuations and anharmonicity in lead iodide perovskites from molecular dynamics supercell simulations," J. Phys. Chem. C **121**, 20729–20738 (2017).

[57] J. S. Bechtel, J. C. Thomas, and A. Van der Ven, "Finite-temperature simulation of anharmonicity and octahedral tilting transitions in halide perovskites," Phys. Rev. Mater. **3**, 113605 (2019).

[58] M. Qin, P. F. Chan, and X. Lu, "A systematic review of metal halide perovskite crystallization and film formation mechanism unveiled by in situ GIWAXS," Adv. Mater. **33**, 2105290 (2021).

[59] Y. Guo, O. Yaffe, D. W. Paley, A. N. Beecher, T. D. Hull, G. Szpak, J. S. Owen, L. E. Brus, and M. A. Pimenta, "Interplay between organic cations and inorganic framework and incommensurability in hybrid lead-halide perovskite $CH_3NH_3PbBr_3$," Phys. Rev. Mater. **1**, 042401 (2017).

[60] Z. Zhao, M. Zhong, W. Zhou, Y. Peng, Y. Yin, D. Tang, and B. Zou, "Simultaneous triplet exciton–phonon and exciton–photon photoluminescence in the individual weak confinement $CsPbBr_3$ micro/nanowires," J. Phys. Chem. C **123**, 25349–25358 (2019).

[61] J. Xue, D. Yang, B. Cai, X. Xu, J. Wang, H. Ma, X. Yu, G. Yuan, Y. Zou, J. Song, and H. Zeng, "Photon-induced reversible phase transition in $CsPbBr_3$ perovskite," Adv. Funct. Mater. **29**, 1807922 (2019).

[62] L. Gao, L. Yadgarov, R. Sharma, R. Korobko, K. M. McCall, D. H. Fabini, C. C. Stoumpos, M. G. Kanatzidis, A. M. Rappe, and O. Yaffe, "Metal cation s lone-pairs increase octahedral tilting instabilities in halide perovskites," Mater. Adv. **2**, 4610–4616 (2021).

[63] C. M. Iaru, A. Brodu, N. J. J. van Hoof, S. E. T. Ter Huurne, J. Buhot, F. Montanarella, S. Buhbut, P. Christianen, D. Vanmaekelbergh, C. de Mello Donega, J. Gómez Rivas, P. M. Koenraad, and A. Y. Silov, "Fröhlich interaction dominated by a single phonon mode in $CsPbBr_3$," Nat. Commun. **12**, 5844 (2021).

[64] J. P. Perdew, K. Burke, and M. Ernzerhof, "Generalized gradient approximation made simple," Phys. Rev. Lett. **77**, 3865 (1996).

[65] S. Grimme, "Semiempirical GGA-type density functional constructed with a long-range dispersion correction," J. Comput. Chem. **27**, 1787–1799 (2006).

[66] S. Grimme, S. Ehrlich, and L. Goerigk, "Effect of the damping function in dispersion corrected density functional theory," J. Comput. Chem. **32**, 1456–1465 (2011).

[67] G. Kresse and J. Hafner, "*Ab initio* molecular dynamics for liquid metals," Phys. Rev. B **47**, 558 (1993).

[68] G. Kresse and J. Furthmüller, "Efficiency of *ab-initio* total energy calculations for metals and semiconductors using a plane-wave basis set," Comput. Mater. Sci. **6**, 15–50 (1996).

[69] G. Kresse and J. Furthmüller, "Efficient iterative schemes for *ab initio* total-energy calculations using a plane-wave basis set," Phys. Rev. B **54**, 11169 (1996).

[70] P. E. Blöchl, "Projector augmented-wave method," Phys. Rev. B **50**, 17953 (1994).

[71] H. J. Monkhorst and J. D. Pack, "Special points for Brillouin-zone integrations," Phys. Rev. B **13**, 5188 (1976).

[72] D. E. P. Vanpoucke, K. Lejaeghere, V. Van Speybroeck, M. Waroquier, and A. Ghysels, "Mechanical properties from periodic plane wave quantum mechanical codes: The challenge of the flexible nanoporous MIL-47(V) framework," J. Phys. Chem. C **119**, 23752–23766 (2015).

[73] A. E. J. Hoffman, I. Senkovska, J. Wieme, A. Krylov, S. Kaskel, and V. Van Speybroeck, "Unfolding the terahertz spectrum of soft porous crystals: Rigid unit modes and their impact on phase transitions," J. Mater. Chem. A **10**, 17254–17266 (2022).

[74] A. Togo and I. Tanaka, "First principles phonon calculations in materials science," Scr. Mater. **108**, 1–5 (2015).

[75] T. D. Kühne, M. Iannuzzi, M. Del Ben, V. V. Rybkin, P. Seewald, F. Stein, T. Laino, R. Z. Khaliullin, O. Schütt, F. Schiffmann, D. Golze, J. Wilhelm, S. Chulkov, M. H. Bani-Hashemian, V. Weber, U. Borštnik, M. Taillefumier, A. S. Jakobovits, A. Lazzaro, H. Pabst, T. Müller, R. Schade, M. Guidon, S. Andermatt, N. Holmberg, G. K. Schenter, A. Hehn, A. Bussy, F. Belleflamme, G. Tabacchi, A. Glöß, M. Lass, I. Bethune, C. J. Mundy, C. Plessl, M. Watkins, J. VandeVondele, M. Krack, and J. Hutter, CP2K: An Electronic Structure

and Molecular Dynamics Software Package - Quickstep: Efficient and Accurate Electronic Structure Calculations.

[76] G. Lippert, J. Hutter, and M. Parrinello, "A hybrid Gaussian and plane wave density functional scheme," Mol. Phys. **92**, 477–488 (1997).

[77] J. VandeVondele and J. Hutter, "Gaussian basis sets for accurate calculations on molecular systems in gas and condensed phases," J. Chem. Phys. **127**, 114105 (2007).

[78] S. Goedecker, M. Teter, and J. Hutter, "Separable dual-space Gaussian pseudopotentials," Phys. Rev. B **54**, 1703 (1996).

[79] G. J. Martyna, M. L. Klein, and M. Tuckerman, "Nosé–Hoover chains: The canonical ensemble via continuous dynamics," J. Chem. Phys. **97**, 2635–2643 (1992).

[80] G. J. Martyna, D. J. Tobias, and M. L. Klein, "Constant pressure molecular dynamics algorithms," J. Chem. Phys. **101**, 4177–4189 (1994).

[81] D.-B. Zhang, T. Sun, and R. M. Wentzcovitch, "Phonon quasiparticles and anharmonic free energy in complex systems," Phys. Rev. Lett. **112**, 058501 (2014).

[82] M. Thomas, M. Brehm, R. Fligg, P. Vöhringer, and B. Kirchner, "Computing vibrational spectra from *ab initio* molecular dynamics," Phys. Chem. Chem. Phys. **15**, 6608–6622 (2013).

[83] S. Borgmans, S. M. J. Rogge, J. S. De Vos, C. V. Stevens, P. Van Der Voort, and V. Van Speybroeck, "Quantifying the likelihood of structural models through a dynamically enhanced powder X-ray diffraction protocol," Angew. Chem., Int. Ed. **60**, 8913–8922 (2021).

[84] V. Favre-Nicolin and R. Černý, "FOX, free objects for crystallography: A modular approach to *ab initio* structure determination from powder diffraction," J. Appl. Crystallogr. **35**, 734–743 (2002).

[85] T. J. Whitcher, L. C. Gomes, D. Zhao, M. Bosman, X. Chi, Y. Wang, A. Carvalho, H. K. Hui, Q. Chang, M. B. H. Breese, A. H. Castro Neto, A. T. S. Wee, H. D. Sun, E. E. M. Chia, and A. Rusydi, "Dual phases of crystalline and electronic structures in the nanocrystalline perovskite $CsPbBr_3$," NPG Asia Mater. **11**, 70 (2019).

[86] Š. Svirskas, S. Balčiūnas, M. Šimėnas, G. Usevičius, M. Kinka, M. Velička, D. Kubicki, M. E. Castillo, A. Karabanov, V. V. Shvartsman, M. de Rosário Soares, V. Šablinskas, A. N. Salak, D. C. Lupascu, and J. Banys, "Phase transitions, screening and dielectric response of $CsPbBr_3$," J. Mater. Chem. A **8**, 14015–14022 (2020).

[87] J. A. Steele, T. Braeckevelt, V. Prakasam, G. Degutis, H. Yuan, H. Jin, E. Solano, P. Puech, S. Basak, M. I. Pintor-Monroy, H. Van Gorp, G. Fleury, R. X. Yang, Z. Lin, H. Huang, E. Debroye, D. Chernyshov, B. Chen, M. Wei, Y. Huo, R. Gehlhaar, J. Genoe, S. De Feyter, S. M. J. Rogge, A. Walsh, E. H. Sargent, P. Yang, J. Hofkens, V. Van Speybroeck, and M. B. J. Roeffaers, "An embedded interfacial network stabilizes inorganic $CsPbI_3$ perovskite thin films," Nat. Commun. **13**, 7513 (2022).

[88] T. Braeckevelt, R. Goeminne, S. Vandenhaute, S. Borgmans, T. Verstraelen, J. A. Steele, M. B. J. Roeffaers, J. Hofkens, S. M. J. Rogge, and V. Van Speybroeck, "Accurately determining the phase transition temperature of $CsPbI_3$ via random-phase approximation calculations and phase-transferable machine learning potentials," Chem. Mater. **34**, 8561–8576 (2022).

[89] A. Maalej, Y. Abid, A. Kallel, A. Daoud, A. Lautié, and F. Romain, "Phase transitions and crystal dynamics in the cubic perovskite $CH_3NH_3PbCl_3$," Solid State Commun. **103**, 279–284 (1997).

[90] M. A. Palafox, "DFT computations on vibrational spectra: Scaling procedures to improve the wavenumbers," Phys. Sci. Rev. **3**, 20170184 (2018).

[91] A. E. J. Hoffman, L. Vanduyfhuys, I. Nevjestić, J. Wieme, S. M. J. Rogge, H. Depauw, P. Van Der Voort, H. Vrielinck, and V. Van Speybroeck, "Elucidating the vibrational fingerprint of the flexible metal–organic framework MIL-53(Al) using a combined experimental/computational approach," J. Phys. Chem. C **122**, 2734–2746 (2018).